International Journal of Marine Engineering Innovation and Research, Vol. 11(1), Mar. 2026. 37-56
(pISSN: 2541-5972, eISSN: 2548-1479)

Effect of Gawn Series Propeller Camber Ratio Variations on Fuel Consumption Using Engine Propeller Matching

Maulana Rakhim[1*], Achmad Baidowi[2], Mahendra Indiarianto[3]
Received: 16 January 2026 / Revised: 2 February 2026 / Accepted: 4 February 2026 / Available Online: 7 March 2026)

***Abstract*—** Propeller blade geometry, particularly the camber ratio, plays a critical role in determining hydrodynamic behavior and fuel consumption in marine propulsion systems. This study investigates the influence of camber ratio variation on the performance of a Gawn Series propeller by applying an Engine–Propeller Matching (EPM) approach. Open-water performance characteristics, including thrust coefficient (KT), torque coefficient (KQ), and open-water efficiency (η_o), were obtained through Computational Fluid Dynamics (CFD) simulations for four camber configurations of 0%, 1%, 1.5%. The numerical model was validated using resistance and open-water test data, yielding deviations below 5% and 3%, respectively, which confirms the reliability of the simulation results. The analysis shows that higher camber ratios generally increase thrust and torque as a result of strengthened pressure gradients and enhanced flow acceleration along the suction side of the blade, with the 1% camber configuration demonstrating the highest efficiency at J = 0.9 (η_o = 0.596), representing a 3.85% improvement over the baseline. Matching the resulting propeller load curves with the performance envelope of a 2 × 3900 kW engine setup provides insight into optimal operating conditions and specific fuel consumption across the vessel's working speed range. The 1% camber variant consistently delivers better fuel economy, maintaining safe operating points. Overall, these results underscore the substantive influence of camber modification on propeller hydrodynamics and propulsion efficiency, identifying the 1% camber configuration as the most suitable option for 60-m high-speed vessels based on combined hydrodynamic, fuel, and operational criteria within the EPM framework.

Keywords— Camber Ratio, Gawn Series Propeller, EPM, CFD, SFOC.

**Corresponding Author: maulanarakhim03@gmail.com*

I. INTRODUCTION

An accurate assessment of propulsion efficiency in marine vessels necessitates a system-level perspective that accounts for the interaction between propeller hydrodynamics and engine performance. The hydrodynamic behavior of the propeller, commonly represented by the thrust coefficient (KT) and torque coefficient (KQ), determines the power demand imposed on the propulsion system under varying operational conditions. However, the resulting fuel consumption is not solely governed by propeller performance, but by how effectively the propeller load characteristics correspond to the available engine power. This interaction is conventionally evaluated using the Engine–Propeller Matching (EPM) approach, which identifies the operating condition at which the engine output is balanced with the propeller power requirement, thereby supporting improved fuel efficiency.

The Gawn–Burrill Series propeller has been extensively applied in high-speed marine vessels, including the 60 m patrol craft considered in this study, and has therefore attracted considerable research interest regarding its hydrodynamic behavior. Previous experimental investigations and Computational Fluid Dynamics (CFD) analyses have consistently reported that propeller geometry, with particular emphasis on the camber ratio, exerts a significant influence on thrust generation, torque characteristics, and the development of flow structures around the blades. These hydrodynamic modifications directly affect the overall efficiency of the propulsion system [1].

Previous studies have examined the influence of camber ratio on propeller performance using various analytical and experimental approaches. Indiaryanto [2] conducted numerical investigations employing a combination of vortex panel and blade element methods to evaluate the effect of camber on thrust and torque characteristics. Experimental evidence was later provided by N. M. Nouri and S. Mohammadi [3] who quantified the impact of camber variation on propeller loading behavior. In addition, Tadros [4] assessed the role of face-side camber in modifying propeller performance and fuel consumption for a bulk carrier operating under calm water conditions. Taken together, these investigations demonstrate that alterations in camber geometry can lead to pronounced changes in propeller hydrodynamics and overall propulsion performance.

Despite the substantial body of research on camber ratio effects, most existing studies remain focused on open-water propeller characteristics and do not explicitly relate geometric modifications to engine fuel consumption. In particular, the linkage between camber

Maulana Rakhim is with Departement of Marine Engineering, Institut Teknologi Sepuluh Nopember, Surabaya, 60111, Indonesia. E-mail: maulanarakhim03@gmail.com
Achmad Baidowi is with Departement of Marine Engineering, Institut Teknologi Sepuluh Nopember, City, 60111, Indonesia. E-mail: ahmadbai@gmail.com
Marhaendra Indiarianto is with Departement of 2. Research Center for Hydrodynamics Technology, National Research and Innovation Agency (BRIN), City, Postal Code, 60117 Country. E-mail: indiaryanto@gmail.com

variation and engine operating behavior has not been sufficiently addressed. To bridge this gap, the present study investigates the influence of camber ratio modifications of a Gawn Series propeller on fuel consumption using an Engine–Propeller Matching (EPM) approach. Open-water performance data obtained from CFD simulations are employed to derive propeller load curves, which are subsequently coupled with the engine performance envelope to identify the corresponding operating points. This framework enables a system-level assessment of how propeller geometric adjustments translate into fuel-efficiency improvements within an integrated propulsion system.

II. METHOD

A. Description

This study utilizes a fast patrol vessel model that had previously undergone physical testing in a towing tank facility. The full-scale vessel has an overall length of 60 meters and is designed to operate at high speeds, incorporating a semi planing hull form optimized to deliver improved hydrodynamic efficiency. The baseline hull geometry was developed from a validated lines plan, ensuring that the numerical representation remains consistent with the actual characteristics of the prototype vessel.

Numerical simulations were performed using a 1:15.03 scale model within a Computational Fluid Dynamics (CFD) framework. The selected scaling ratio provides a balanced compromise between geometric fidelity and computational efficiency while preserving the hydrodynamic similarity required for reliable flow predictions. The principal dimensions and geometric configuration of the fast patrol vessel employed in this study are summarized in **table 1** and Figure. 1. **3D models of the fast patrol vessel (a) and symmetrical blade propeller****Figure. 1**.

TABLE 1
MAIN DIMENSION OF SHIP MODEL

Parameter	Size		Unit
	Full Scale	Model Scale	
Scale Ratio		1 : 15.03	
LOA	59.543	3.962	LOA
Lwl	54.032	3.654	Lwl
Bm	8.100	0.539	Bm
D	4.900	0.326	D
T	2.570	0.171	T

Figure 1 show fast patrol vessel (a) and symmetrical blade propeller (b) 3D model. The resistance test results of the high-speed patrol vessel were first employed to validate the Computational Fluid Dynamics (CFD) simulations. This validation step ensures that the numerical predictions accurately represent the physical behavior observed during the towing tank experiments before they are used in subsequent analyses. Once validated, the numerical model was further utilized to examine the influence of varying propeller foil camber on the ship's resistance characteristics affect fuel consumption through an Engine Propeller Matching approach.

On the other hand, a propeller model with a geometric scale of 1:15.03 was fabricated to support open water experiments conducted in the laboratory, as summarized in TABLE 2. The same scaled geometry was adopted in the numerical simulations, where the hydrodynamic performance of the propeller was evaluated using a CFD-based approach. The use of a scaled propeller model not only preserves geometric similarity and hydrodynamic fidelity relative to the full-scale configuration, but also significantly reduces the computational demand. A smaller geometric scale results in fewer mesh elements, shorter processing times, and a more efficient use of computational resources, while still capturing the essential flow phenomena required for performance analysis [5].

TABLE 2
MAIN DIMENSION OF PROPELLER

Dimension	**Full scale**	**Scaled (1:15.03)**
Diameter (mm)	116,43	1750
Number of blades	4	4
Expanded area ratio	0,828	0,828
Pitch ratio	1,380	1,380
Rotation (rpm)	2132	550

B. Computational Domain and Boundary Conditions

To support the numerical analysis conducted using the CFD approach, input data derived from the open-water tests of propellers with various camber ratios were required as performance parameters. The CFD simulations of the propeller in open-water conditions were carried out within a carefully defined computational domain, as the accuracy and numerical stability of the solution are strongly influenced by the domain configuration. The domain dimensions were established in accordance with the ITTC [6] recommendations, using a propeller with a diameter of 116.43 mm, where all boundaries were expressed in multiples of the propeller diameter (D). The propeller center was positioned 2D downstream of the inlet, while the outlet boundary was placed 6D downstream from the propeller plane. The lateral cylindrical boundary had a diameter of 6D, ensuring that the computational space was sufficiently broad to capture the flow development, pressure field, and fluidstructure interaction without

introducing artificial confinement effects.

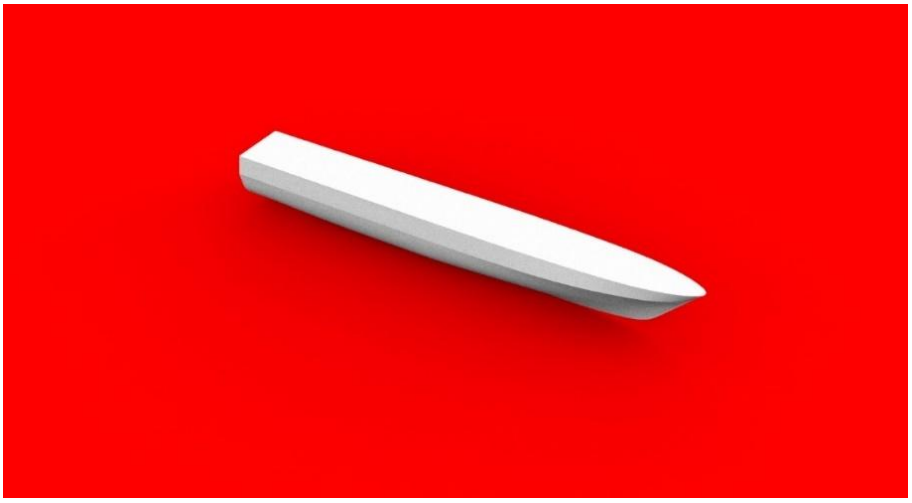

(a)

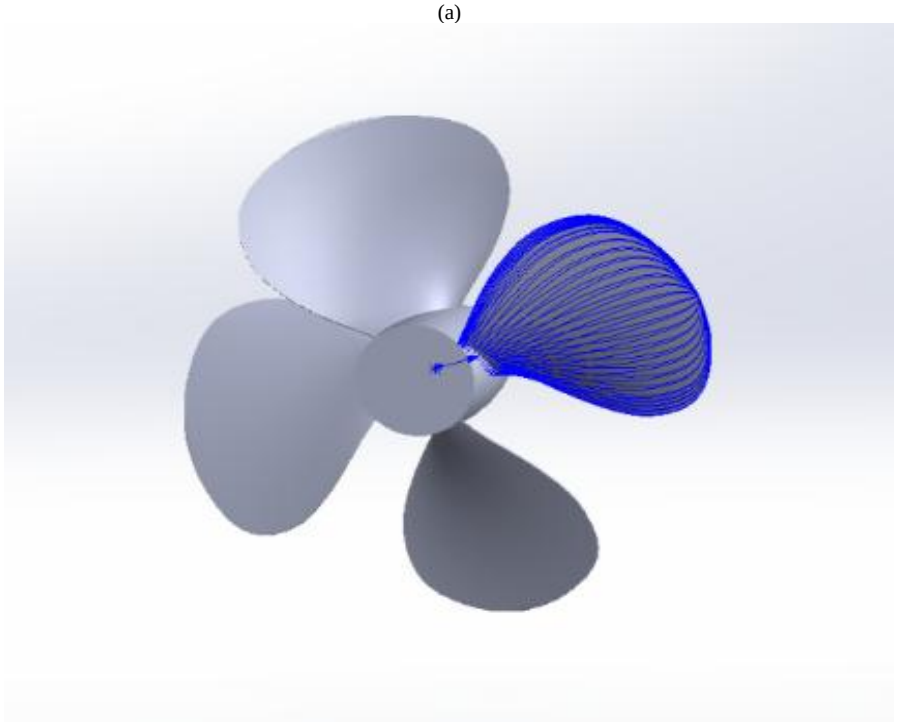

(b)

Figure. 1. 3D models of the fast patrol vessel (a) and symmetrical blade propeller (b)

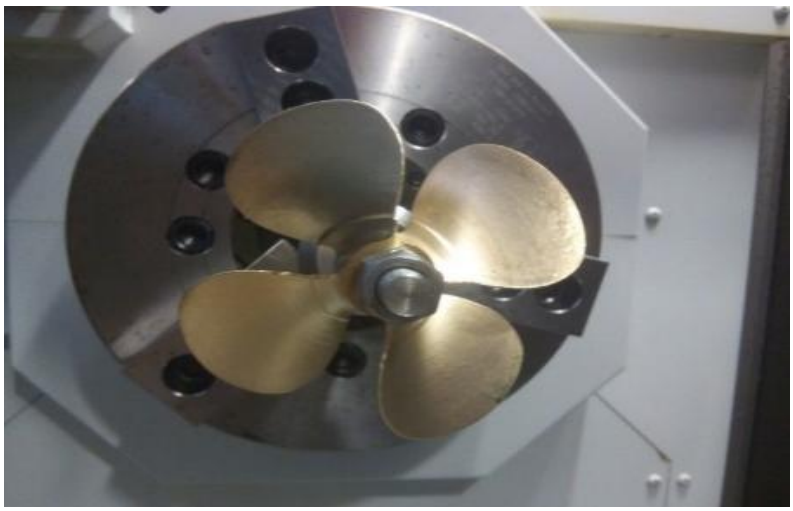

Figure. 2. Symmetrical blade propeller (Gawn–Burrill series) model for the open-water test

Figure. 3. The symmetrical blade propeller (Gawn–Burrill series) used in the open-water test at the Hydrodynamics Laboratory of BRIN, Surabaya, Indonesia

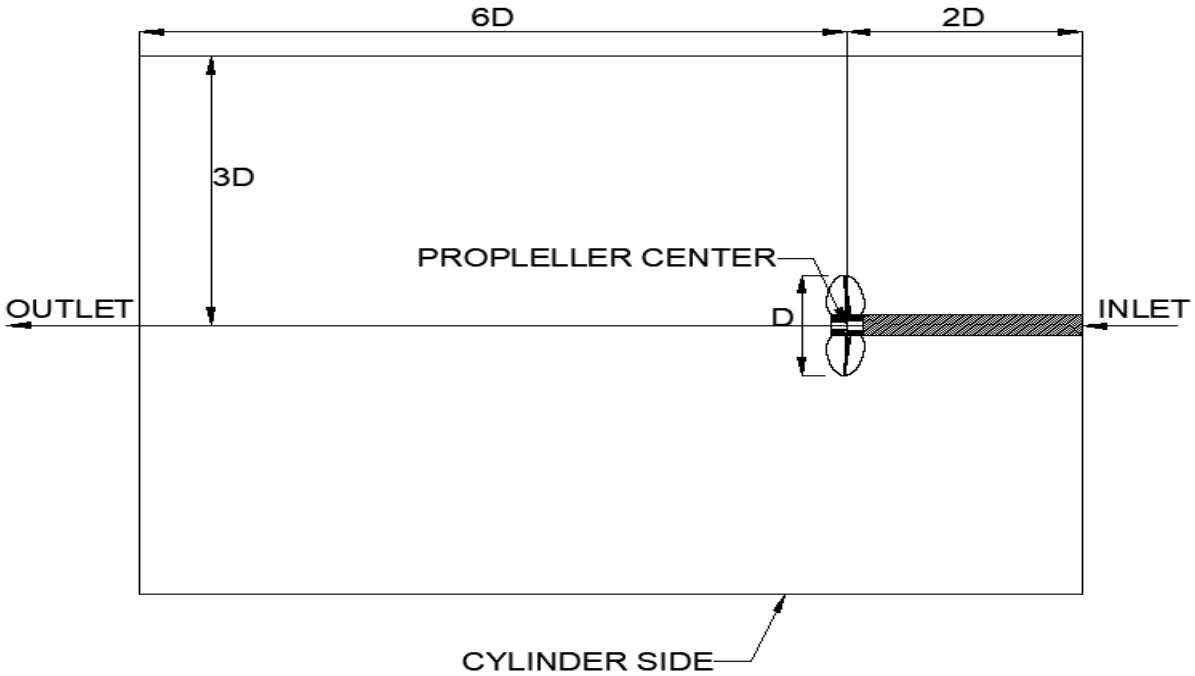

Figure. 4. Computational domain and boundary conditions of the propeller model

Boundary conditions were defined to accurately represent the interaction between the fluid and the computational domain. Velocity and pressure were imposed as far-field conditions at the inlet and cylindrical sidewalls, whereas a fixed pressure of 0 bar was applied at the outlet. A slip condition was assigned to the propeller shaft, ensuring zero tangential shear stress along the rotating axis. Meanwhile, wall functions were applied on the propeller blade surfaces to properly resolve the near-wall boundary layer effect.

For the CFD setup used in the resistance test Figure 8, the computational domain was constructed in accordance with the ITTC Recommended Procedures and Guidelines [6] to maintain domain independence and eliminate boundary-related flow interference. The ship model, having a waterline length (LWL) of 3651.4 mm, served as the reference scale for determining all domain dimensions, each defined as a multiple of the model length.

The model was placed symmetrically within the domain, with a distance of 2L upstream of the inlet to allow the incoming flow to fully develop before reaching the hull. Downstream, the outlet was positioned 5L from the stern, resulting in a total domain length of 7L. Vertically, the distance between the keel and the bottom boundary was set to 2L, while the free surface was

positioned 3L above the model centerline to accommodate wave elevations generated during the resistance test. In the transverse direction, the sidewall boundaries were placed 2L from the ship hull and 3L from the top opening, minimizing reflections and ensuring that blockage and domain-induced disturbances did not influence the flow field around the ship

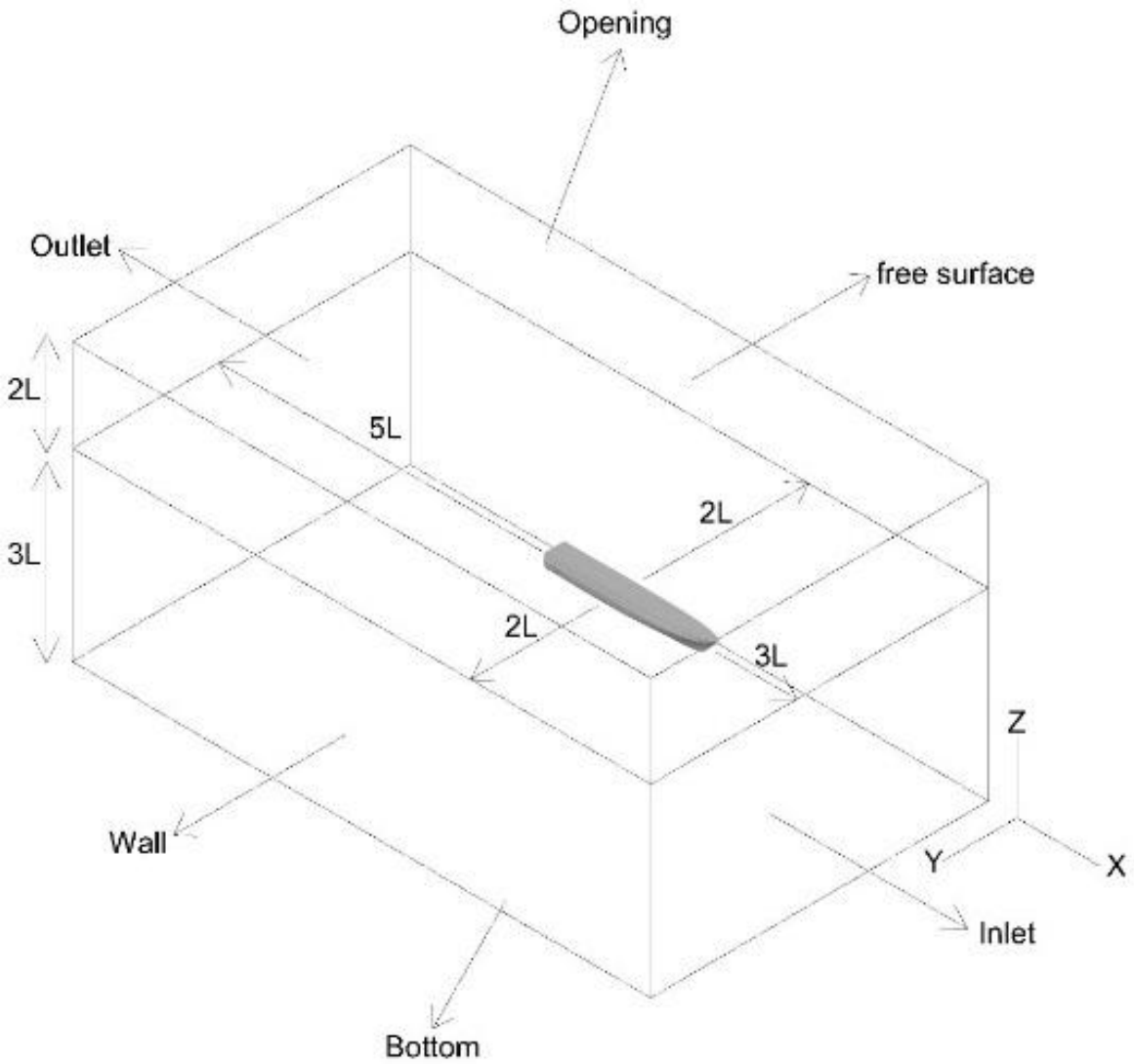

Figure. 5. Computational domain and boundary conditions of the hull model

The boundary conditions in this simulation were defined as follows. The upstream region of the domain was assigned as the inlet with a uniform velocity profile, while the downstream region was treated as an outlet by applying a zero-gradient condition to the flow variables. The upper boundary of the domain was specified as an opening, allowing the pressure and velocity fields to adjust naturally according to the flow conditions. Meanwhile, the bottom and side boundaries of the domain were modeled as fixed no-slip walls. The free surface was represented using a two-phase interface to capture the interaction between water and air.

This configuration of boundary conditions ensures that the flow field around the ship geometry develops in a stable and physically consistent manner, while minimizing numerical reflections and boundary induced disturbances that could affect the accuracy of the simulation.

C. *Configuration of Camber Ratio Variations on Foil Propeller*

The evaluation of the symmetrical blade propeller performance was carried out by introducing several camber ratio modifications to the foil section. This approach, which has long been adopted in aeronautical and hydrodynamic design studies, alters the meanline geometry of the foil and produces an asymmetry between the upper and lower surfaces [7]. A foil is defined as having positive camber when the upper surface exhibits greater curvature than the lower surface. Such geometric adjustment has been shown to enhance the hydrodynamic characteristics of marine propellers by increasing sectional lift and improving flow development over the blade surface.

Variations in camber ratio not only influence the pressure distribution but also modify the flow patterns around the blade, which collectively contribute to

changes in thrust generation and overall propulsive efficiency. The camber configurations considered in this study are summarized in Table 3, meanwhile Figure 5 representing the proportional relationship between the foil's curvature and chord length as the basis for hydrodynamic performance assessment.

Experimental open water test data were further employed to validate the CFD predictions for the propeller with a 0% camber ratio. This comparison ensures that the numerical model accurately reproduces the hydrodynamic behavior observed in laboratory measurements, thereby establishing confidence in the subsequent analyses involving modified camber configurations.

TABLE 3
CAMBER RATIO VARIATION

Camber ratio (f/c)	0%	1%	1.5%	2.5%

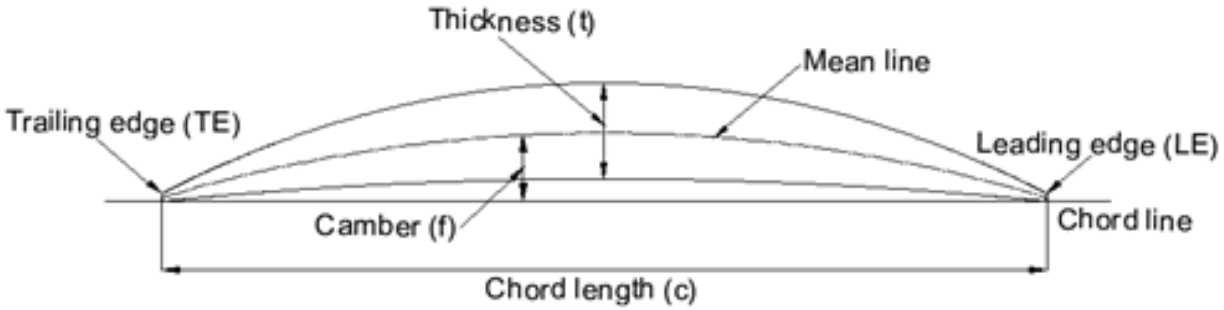

Figure. 6. Geometric parameters of the propeller foil

The experimental open-water data served as the primary reference for validating the CFD predictions obtained for the foil configuration with a 0% camber ratio. A direct comparison between the measured open-water performance and the CFD simulated results was conducted to evaluate the degree of agreement between both datasets. This validation step was essential to confirm that the numerical model was capable of reproducing the hydrodynamic characteristics of the propeller with sufficient accuracy before extending the analysis to cambered configurations.

D. Goovering Equation

The Navier–Stokes equations form the fundamental basis for fluid dynamics analysis, as they describe the balance of forces acting on an infinitesimal fluid element. These equations account for inertia, pressure gradients, viscous stresses, and gravitational effects in the three coordinate directions. The velocity components u, v, and w represent the local flow velocities along the x, y, and z axes, respectively. For incompressible flow, the governing equations consist of the continuity equation together with the momentum equations, which can be expressed as follows:

$$\left(\frac{\partial u}{\partial x}+\frac{\partial v}{\partial y}+\frac{\partial w}{\partial z}\right)=0 \qquad 1)$$

The momentum equations in the x, y, and z directions further illustrate how fluid motion is governed by the concurrent action of several fundamental forces. These include the inertial forces, gravitational force, pressure gradients, and viscous forces that account for internal fluid friction. The interaction among these components determines the local flow behaviour.

$$\rho\left(\frac{\partial u}{\partial t}+u\frac{\partial u}{\partial x}+v\frac{\partial u}{\partial y}+w\frac{\partial u}{\partial z}\right)=\rho g_x-\frac{\partial P}{\partial x}$$
$$+\mu\left(\frac{\partial^2 u}{\partial x^2}+\frac{\partial^2 u}{\partial y^2}+\frac{\partial^2 u}{\partial z^2}\right) \qquad (2)$$
$$\rho\left(\frac{\partial v}{\partial t}+u\frac{\partial v}{\partial x}+v\frac{\partial v}{\partial y}+w\frac{\partial v}{\partial z}\right)=\rho g_y-\frac{\partial P}{\partial y}$$
$$+\mu\left(\frac{\partial^2 v}{\partial x^2}+\frac{\partial^2 v}{\partial y^2}+\frac{\partial^2 v}{\partial z^2}\right)$$
$$\rho\left(\frac{\partial w}{\partial t}+u\frac{\partial w}{\partial x}+v\frac{\partial w}{\partial y}+w\frac{\partial w}{\partial z}\right)=\rho g_z-\frac{\partial P}{\partial z}$$
$$+\mu\left(\frac{\partial^2 w}{\partial x^2}+\frac{\partial^2 w}{\partial y^2}+\frac{\partial^2 w}{\partial z^2}\right)$$

In turbulent flows, the instantaneous fluid velocity exhibits random fluctuations that introduce additional stresses originating from turbulent effects. To capture this behavior, the Navier Stokes equations are reformulated into the Reynolds-Averaged Navier Stokes (RANS) form, in which each velocity component is decomposed into its mean value and a fluctuating part. This averaging process generates an extra term $\partial/(\partial x_i)(\rho u_i' u_j')$, commonly known as the Reynolds stress tensor, which represents the momentum transfer associated with turbulent velocity fluctuations.

$$\rho\left(\frac{\partial u}{\partial t}+u\frac{\partial u}{\partial x}+v\frac{\partial u}{\partial y}+w\frac{\partial u}{\partial z}\right)=\rho g_x-\frac{\partial P}{\partial x}$$
$$+\mu\left(\frac{\partial^2 u}{\partial x^2}+\frac{\partial^2 u}{\partial y^2}+\frac{\partial^2 u}{\partial z^2}\right)-\frac{\partial}{\partial x}\left(\overline{\rho u'u'}\right)-\frac{\partial}{\partial y}$$
$$\left(\overline{\rho u'v'}\right)-\frac{\partial}{\partial z}\left(\overline{\rho u'w'}\right) \qquad (3)$$
$$\rho\left(\frac{\partial u}{\partial t}+u\frac{\partial u}{\partial x}+v\frac{\partial u}{\partial y}+w\frac{\partial u}{\partial z}\right)=\rho g_y-\frac{\partial P}{\partial y}$$
$$+\mu\left(\frac{\partial^2 u}{\partial x^2}+\frac{\partial^2 u}{\partial y^2}+\frac{\partial^2 u}{\partial z^2}\right)-\frac{\partial}{\partial x}\left(\overline{\rho v'u'}\right)-\frac{\partial}{\partial y}$$

$$(\overline{\rho v'v'}) - \frac{\partial}{\partial z}(\overline{\rho v'w'})$$
$$\rho\left(\frac{\partial u}{\partial t} + u\frac{\partial u}{\partial x} + v\frac{\partial u}{\partial y} + w\frac{\partial u}{\partial z}\right) = \rho g_z - \frac{\partial P}{\partial z}$$
$$+\mu\left(\frac{\partial^2 u}{\partial x^2} + \frac{\partial^2 u}{\partial y^2} + \frac{\partial^2 u}{\partial z^2}\right) - \frac{\partial}{\partial x}(\overline{\rho w'u'}) - \frac{\partial}{\partial y}$$
$$(\overline{\rho w'v'}) - \frac{\partial}{\partial z}(\overline{\rho w'w'})$$

Terms such as ρu′u′, ρu′v′, and ρu′w′ represent the components of the Reynolds stress tensor, which describe the influence of velocity fluctuations on the mean momentum field in turbulent flows. These additional terms play a crucial role in turbulence modeling, as they capture the momentum transfer generated by small scale turbulence that cannot be resolved directly in practical CFD simulations.

In the verification procedure for both the resistance test and the open water analysis, different turbulence model configurations were employed to accommodate the distinct flow characteristics encountered around the ship hull and the propeller. This distinction is necessary because the spatial distribution of Reynolds stresses varies significantly between the two cases, primarily due to differences in turbulent viscosity and local velocity gradients.

Within the Reynolds Averaged Navier Stokes (RANS) framework used for the ship model, the closure of Reynolds stresses is achieved through an eddy viscosity approach. In this formulation, the turbulent viscosity (ν_t) is evaluated using the parameters derived from the two-equation k–ω model, which solves transport equations for the turbulent kinetic energy (k) and the specific dissipation rate (ω), following the formulation proposed by Wilcox [8]. The relationship between ν_t and these turbulence quantities is expressed as follows

Terms such as ρu′u′, ρu′v′, and ρu′w′ represent the components of the Reynolds stress tensor, which describe the influence of velocity fluctuations on the mean momentum field in turbulent flows. These additional terms play a crucial role in turbulence modeling, as they capture the momentum transfer generated by small scale turbulence that cannot be resolved directly in practical CFD simulations.

In the verification procedure for both the resistance test and the open water analysis, different turbulence model configurations were employed to accommodate the distinct flow characteristics encountered around the ship hull and the propeller. This distinction is necessary because the spatial distribution of Reynolds stresses varies significantly between the two cases, primarily due to differences in turbulent viscosity and local velocity gradients.

Within the Reynolds Averaged Navier Stokes (RANS) framework used for the ship model, the closure of Reynolds stresses is achieved through an eddy viscosity approach. In this formulation, the turbulent viscosity (ν_t) is evaluated using the parameters derived from the two-equation k–ω model, which solves transport equations for the turbulent kinetic energy (k) and the specific dissipation rate (ω), following the formulation proposed by Wilcox [8]. The relationship between ν_t and these turbulence quantities is expressed as follows:

$$v_t = \frac{k}{\omega} \quad (4)$$

To determine the value of ν_t, two additional transport equations are required, which can be written as follows:

$$\frac{\partial k}{\partial t} + \bar{u}_j\frac{\partial k}{\partial x_j} = P_k - \beta^* k\omega + \frac{\partial}{\partial x_j}\left[(v + \sigma_k^* v_t)\frac{\partial k}{\partial x_j}\right] \quad (5)$$

$$\frac{\partial \omega}{\partial t} + \bar{u}_j\frac{\partial \omega}{\partial x_j} = \alpha\frac{\omega}{k}P_k - \beta\omega^2 + \frac{\partial}{\partial x_j}\left[(v + \sigma_\omega^* v_t)\frac{\partial \omega}{\partial x_j}\right] \quad (6)$$

In this formulation, $P_k = \nu_t(\frac{\partial \bar{u}_i}{\partial x_j} + \frac{\partial \bar{u}_j}{\partial x_i})\frac{\partial \bar{u}_i}{\partial x_j}$ represents the production rate of turbulent kinetic energy. The model constants adopted in the Wilcox formulation are $\alpha = \frac{5}{9}, \beta = \frac{3}{40}, \beta^* = 0.09, \sigma_k = 2.0$, and $\sigma_\omega = 2.0$.

In this study, the Reynolds stress tensor is formulated to capture the influence of turbulence on the flow field around the propeller. Following earlier work, such as that of Indiaryanto et al. [9], the Reynolds stresses in the RANS formulation for the open-water simulations were modeled using the Explicit Algebraic Stress Model (EASM). The model, originally developed by Deng et al. [10], provides an algebraic representation of stress anisotropy by directly linking the Reynolds stress tensor to the mean strain rate components.

$$\tau_{ij} = \frac{2}{3}k\delta_{ij} - 2v_t\left[S_{ij} + a_2a_4(S_{ik}W_{kj} - S_{ik}W_{kj}) - 2a_3a_4\left(S_{ik}S_{kj} - \frac{1}{3}S_{mn}S_{mn}\delta_{ij}\right)\right] \quad (7)$$

In this formulation, τ_{ij} represents the Reynolds stress tensor, k denotes the turbulent kinetic energy, and ν_t is the turbulent eddy viscosity. The term S_{ij} corresponds to the mean strain-rate tensor, while δ_{ij} is the Kronecker delta and W_{ij} denotes the mean vorticity tensor. The coefficients a_2, a_3, and a_4 are empirical constants obtained through calibration against experimental measurements or Direct Numerical Simulation (DNS) data. These constants regulate the contribution of strain rotation interactions to the anisotropy of Reynolds stresses.

E. Grid Independence Test

Mesh generation represents a critical stage in CFD simulations, as the discretization quality strongly influences numerical accuracy, solution stability, and the ability of the solver to reach convergence [11]. As illustrated in **Figure. 7** (a) and (b) a highly refined mesh is applied in the regions surrounding the propeller, where steep velocity gradients and complex flow interactions are expected to occur. In contrast, the outer regions of the computational domain are discretized with progressively coarser grid elements to reduce computational cost while maintaining an adequate resolution of the far field flow.

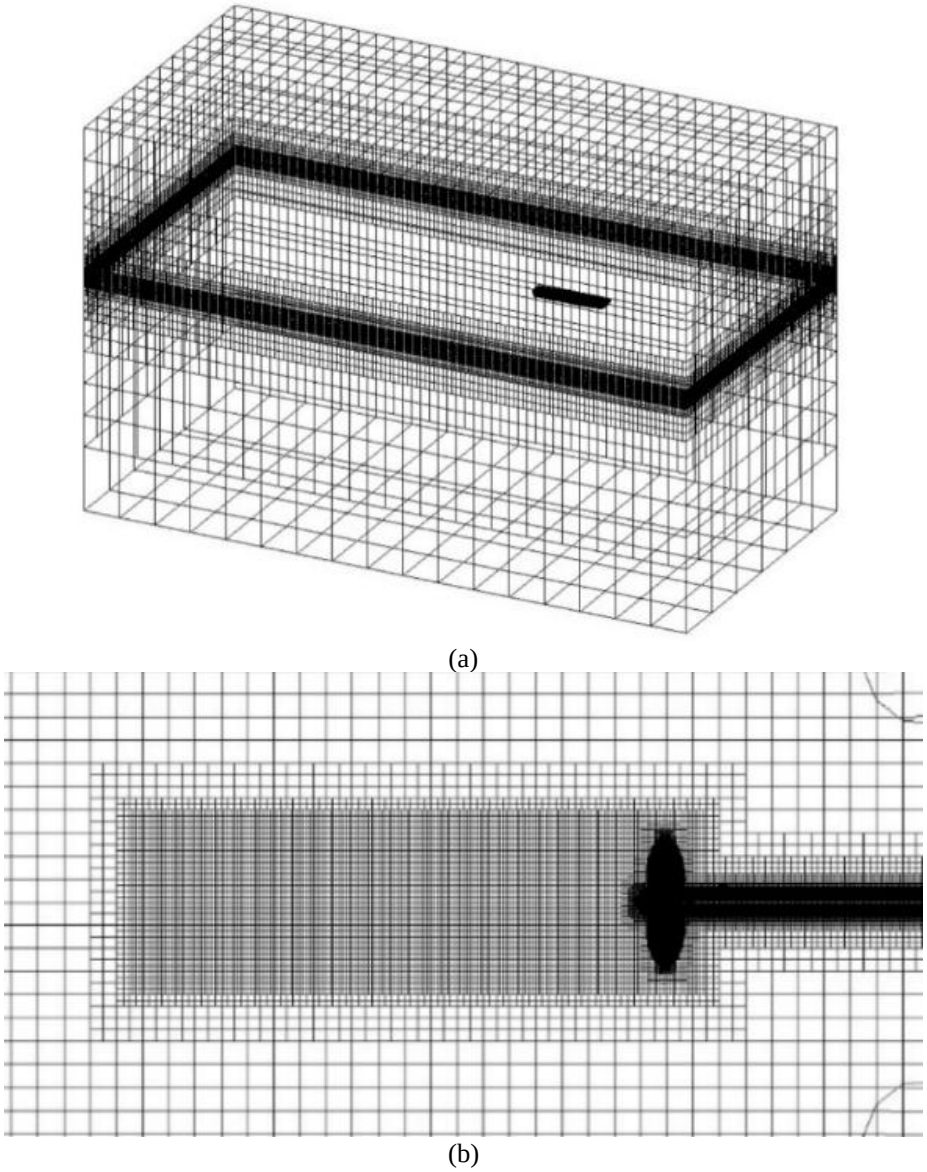

Figure. 7. Mesh configuration of the hull (a) and propeller models (b)

A grid independence assessment was performed by comparing the thrust coefficient (KT) obtained from successive simulations, where the number of cells in each subsequent run was increased to approximately twice that of the previous mesh. The results presented in Table 4 indicate a consistent reduction in KT as the cell count increases, a trend that is also depicted in Figure 10. As the mesh is progressively refined, the KT values approach an asymptotic limit of approximately 0.277.

In this study, a maximum deviation threshold of 2% was adopted as the criterion for establishing grid independence [12]. The comparison between Run 4 (N = 3,096,382 cells) and Run 3 (N = 1,993,017 cells) yields a difference of only 0.29%, indicating that both simulations already fall within the acceptable tolerance. Based on these findings, the mesh configuration with 1,993,017 cells was selected as the optimal grid for subsequent propeller simulations, providing a balance between numerical accuracy and computational efficiency.

TABLE 4
OPEN WATER GRID INDEPENDENT TEST

Number of element	Kt	Percentage difference
604,193	0.287	-
1,050,580	0.282	2.01%
1,993,017	0.278	1.39%
3,096,382	0.277	0.29%

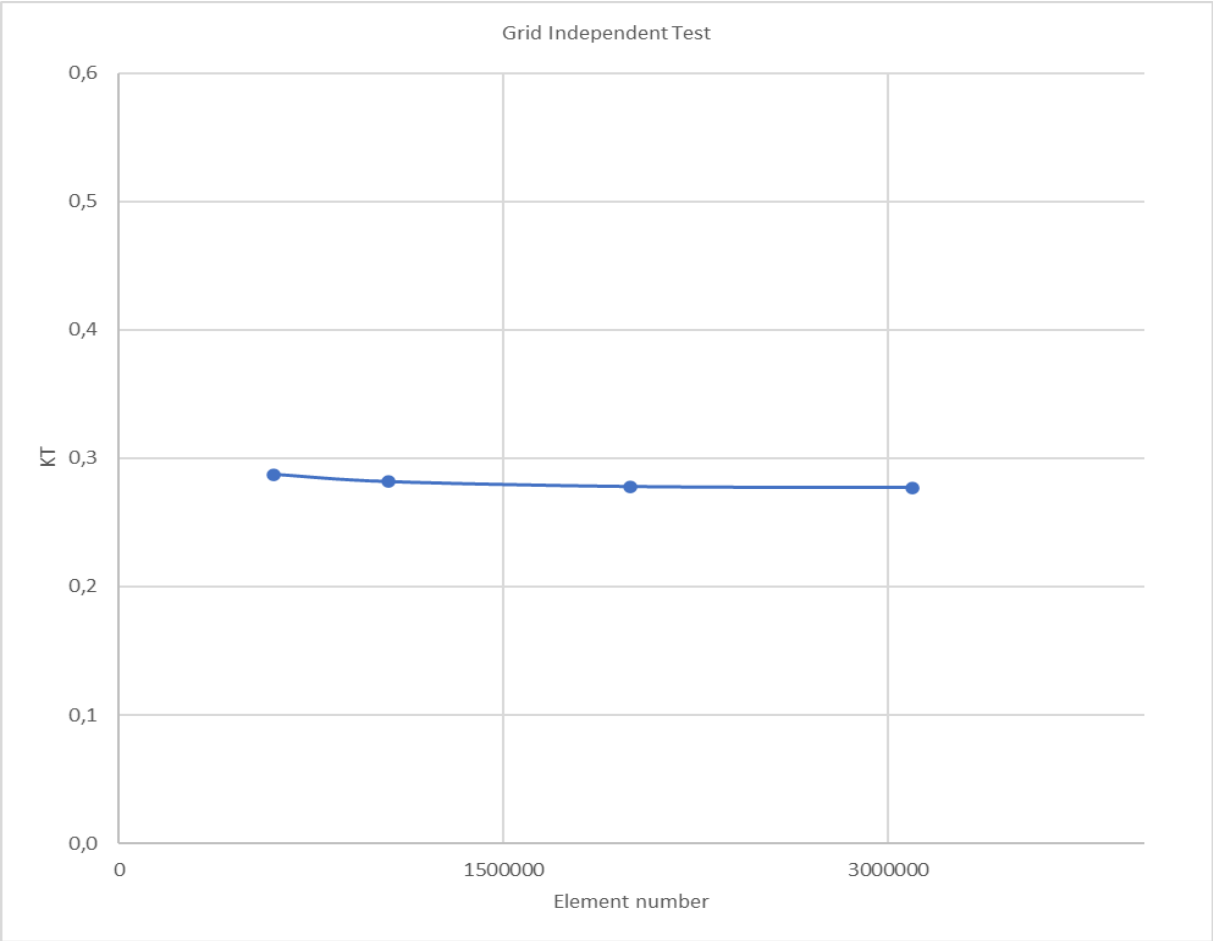

Figure. 8. Grid Independence test for symmetrical blade propeller

The grid-independence assessment for the resistance test was carried out at a ship speed of 28 knots. This operating condition was selected to ensure that both the ship's forward velocity and the propeller operating point represent the typical performance range required for numerical evaluation. The results of the grid independence test are presented in TABLE 5 below

TABLE 5
RESSISTANCE GRID INDEPENDENT TEST

Number of cells	Resistance coefficient	Percentage different
2050572	0.1409	-
3087904	0.1437	1.9%
4000878	0.1414	1.6%
5377264	0.1417	0.2%

A maximum deviation threshold of 2% was applied as the acceptance criterion for mesh convergence. The percentage differences obtained from the second, third, and fourth mesh configurations—consisting of 2,050,572, 4,000,878, and 5,377,264 cells, respectively were consistently within this tolerance, with deviations of 1.9%, 1.6%, and 0.2%. Among these cases, the second mesh configuration was selected as the optimal choice because it provides a stable resistance coefficient while maintaining computational efficiency.

F. Validation

To evaluate the reliability of the numerical predictions, the CFD simulation results were validated using open-water test data obtained from a 60-meter patrol vessel propeller. The experimental measurements served as a benchmark for assessing the accuracy of the numerical model, particularly for the configuration with a camber ratio of 0%. This validation step ensures that the hydrodynamic characteristics produced by the CFD framework are consistent with the physical behavior exhibited during laboratory testing, thereby establishing a solid basis for the subsequent analysis of camber-induced performance variations.

G. Comparison of Resistance Test Results and CFD Simulations

In the resistance simulation conducted for validation purposes, a maximum deviation of 5% was established as the acceptance threshold for the CFD results. **table 6** presents the comparison between the CFD-predicted resistance values and the results of the towing tank tests.

TABLE 6
RESSISTANCE TEST

No	VM (m/s)	Towing Tank RTM (kN)	RTM CFD (kN)
1	3.45	94.92	91.363
2	3.583	99.24	96.799
3	3.715	103.86	102.501
4	3.848	108.14	108.509
5	3.981	112.38	114.9
Average difference			0.862%

Based on the resistance test validation summarized in Table 6, the average percentage deviation of the total resistance is 0.862%. This deviation falls well within the acceptance criterion of less than 5%, indicating that the CFD resistance predictions exhibit strong agreement with the towing tank experimental measurements.

H. Propeller Coefficients

The hydrodynamic characteristics of the propeller were evaluated using a set of nondimensional performance parameters, namely the advance coefficient (J), thrust coefficient (KT), torque coefficient (KQ), and overall efficiency (η). These key parameters KT, KQ, and η are expressed as functions of J and presented in the form of propeller performance curves. Such representations enable a comprehensive assessment of the propeller's behavior across various operating conditions.

$$J = \frac{V}{nD} \tag{8}$$

$$K_T = \frac{T}{\rho n^2 D^4} \tag{9}$$

$$K_Q = \frac{Q}{\rho n^2 D^5} \tag{10}$$

$$\eta_0 = \frac{K_T J}{2\pi K_Q} \tag{11}$$

In these formulations, V_adenotes the advance velocity (m/s), nis the propeller rotational speed (rpm), Drepresents the propeller diameter (m), Tis the generated thrust (N), Qis the torque (Nm), and ρis the fluid density (kg/m³). These parameters are subsequently expressed as functions of the advance coefficient J, forming the propeller performance curves that serve as the basis for validation and hydrodynamic performance assessment.

I. Comparison of Open Water Test Results and CFD Simulations

In the resistance simulation conducted for validation purposes, a maximum deviation of 5% was established as the acceptance threshold for the CFD results. **Table 6** presents the comparison between the CFD-predicted resistance values and the results of the towing tank tests.

TABLE 7
RESSISTANCE TEST

No	VM (m/s)	Towing Tank RTM (kN)	RTM CFD (kN)
1	3.45	94.92	91.363
2	3.583	99.24	96.799
3	3.715	103.86	102.501
4	3.848	108.14	108.509
5	3.981	112.38	114.9
Selisih rata-rata			0.862%

Based on the resistance test validation summarized in TABLE 7, the average percentage deviation of the total resistance is 0.862%. This deviation falls well within the acceptance criterion of less than 5%, indicating that the CFD resistance predictions exhibit strong agreement with the towing tank experimental measurements.

J. Propeller Coefficients

The hydrodynamic characteristics of the propeller were evaluated using a set of nondimensional performance parameters, namely the advance coefficient (J), thrust coefficient (KT), torque coefficient (KQ), and overall efficiency (η). These key parameters KT, KQ, and η are expressed as functions of J and presented in the form of propeller performance curves. Such representations enable a comprehensive assessment of the propeller's behavior across various operating conditions.

$$J = \frac{V}{nD} \tag{12}$$

$$K_T = \frac{T}{\rho n^2 D^4} \tag{13}$$

$$K_Q = \frac{Q}{\rho n^2 D^5} \tag{14}$$

$$\eta_0 = \frac{K_T J}{2\pi K_Q} \tag{15}$$

In these formulations, V_adenotes the advance velocity (m/s), nis the propeller rotational speed (rpm), Drepresents the propeller diameter (m), Tis the generated thrust (N), Qis the torque (Nm), and ρis the fluid density (kg/m³). These parameters are subsequently expressed as functions of the advance coefficient J, forming the propeller performance curves that serve as the basis for validation and hydrodynamic performance assessment.

K. Comparison of Open Water Test Results and CFD Simulations

The open-water propeller test was conducted at a ship speed of 28 knots to obtain experimental data for validation purposes. Under full-scale operating conditions, the propeller rotates at 550 rpm, corresponding to an advance coefficient of J = 0.9. This value of J lies within the range where the propeller achieves its optimal hydrodynamic efficiency for the designated design configuration.

Figure 11 presents a comparison between the propeller performance curves obtained from laboratory measurements and those predicted by the CFD simulations. The curves include the thrust coefficient (KT), torque coefficient (KQ), and open-water efficiency (η_0), each plotted as a function of the advance coefficient J. This comparison is used to evaluate the accuracy of the CFD hydrodynamic predictions and to validate the consistency of the numerical model against the experimental results.

L. Comparison of Open Water Test Results and CFD Simulations

The open-water propeller test was conducted at a ship speed of 28 knots to obtain experimental data for validation purposes. Under full-scale operating conditions, the propeller rotates at 550 rpm, corresponding to an advance coefficient of J = 0.9. This value of J lies within the range where the propeller achieves its optimal hydrodynamic efficiency for the designated design configuration.

Figure. 9 presents a comparison between the propeller performance curves obtained from laboratory measurements and those predicted by the CFD simulations. The curves include the thrust coefficient (KT), torque coefficient (KQ), and open-water efficiency (η_0), each plotted as a function of the advance coefficient J. This comparison is used to evaluate the accuracy of the CFD hydrodynamic predictions and to validate the consistency of the numerical model against the experimental results.

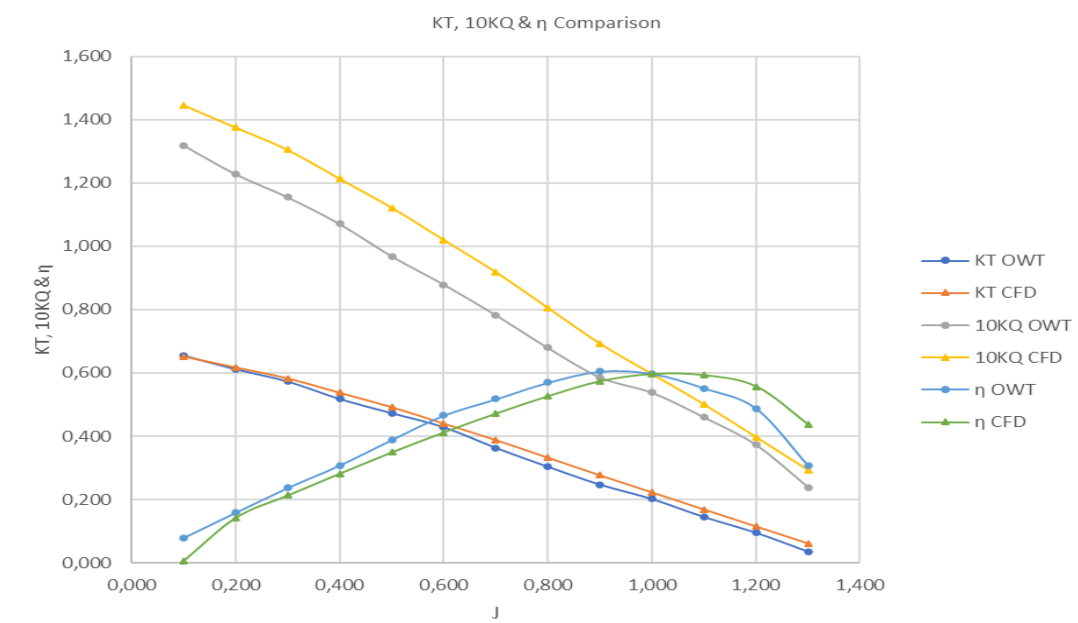

Figure. 9. Comparison of KT, KQ and η obtained from open water propeller test and CFD simulations for 0% camber ratio

The average deviation between the open-water test results and the CFD predictions was found to be 2.88% for K_t, 2.97% for K_φ, and 1.46% for the open-water efficiency (η). These differences each remaining below 3% indicate that the CFD methodology employed in this study provides a high level of accuracy and can reliably represent the hydrodynamic behavior of the propeller [13]. The percentage deviations for K_t, K_φ, and η were computed using the following expression.

$$KT = \frac{1}{N}\sum K_{T_{CFD}} - K_{T_{Test}} \tag{16}$$

$$KT = \frac{1}{N}\sum K_{Q_{CFD}} - K_{Q_{Test}} \tag{17}$$

$$KT = \frac{1}{N}\sum \eta_{CFD} - \eta_{Test} \tag{18}$$

M. Comparison of Open Water Test Results for Each Camber Ratio Variation

Figure. 10, Figure. 11, and **Figure. 12** present the KT, KQ, and open-water efficiency (η) curves, respectively, as functions of the advance coefficient J for all camber ratio variations evaluated through CFD simulations. Overall, increasing the camber ratio leads to higher thrust and torque, as reflected in the increased KT and KQ values shown in Figure 12 and Figure 13. This tendency is consistent with the aerodynamic effect of camber, which enhances sectional lift on the blade profile and consequently increases the generated thrust. However, a higher camber ratio also induces additional drag, resulting in a corresponding increase in KQ.

Figure 14 shows that the 1% camber variation yields the highest open-water efficiency (η_o) among all tested configurations. This result indicates that, at a camber ratio of 1%, the increase in thrust remains more dominant than the rise in torque, allowing the ratio K_T/K_Qto reach its optimum value within the operating J range. In other words, the 1% camber configuration provides the most favorable balance between additional lift and the accompanying drag penalty, resulting in the highest propulsive efficiency.

These findings align with the Engine–Propeller Matching (EPM) assessment discussed previously, where the 1% camber configuration demonstrated a stable operating point, favorable efficiency at high rotational speeds, and improved fuel consumption characteristics. This consistency further reinforces that the 1% camber ratio is the most effective configuration for the propeller design investigated in this study.

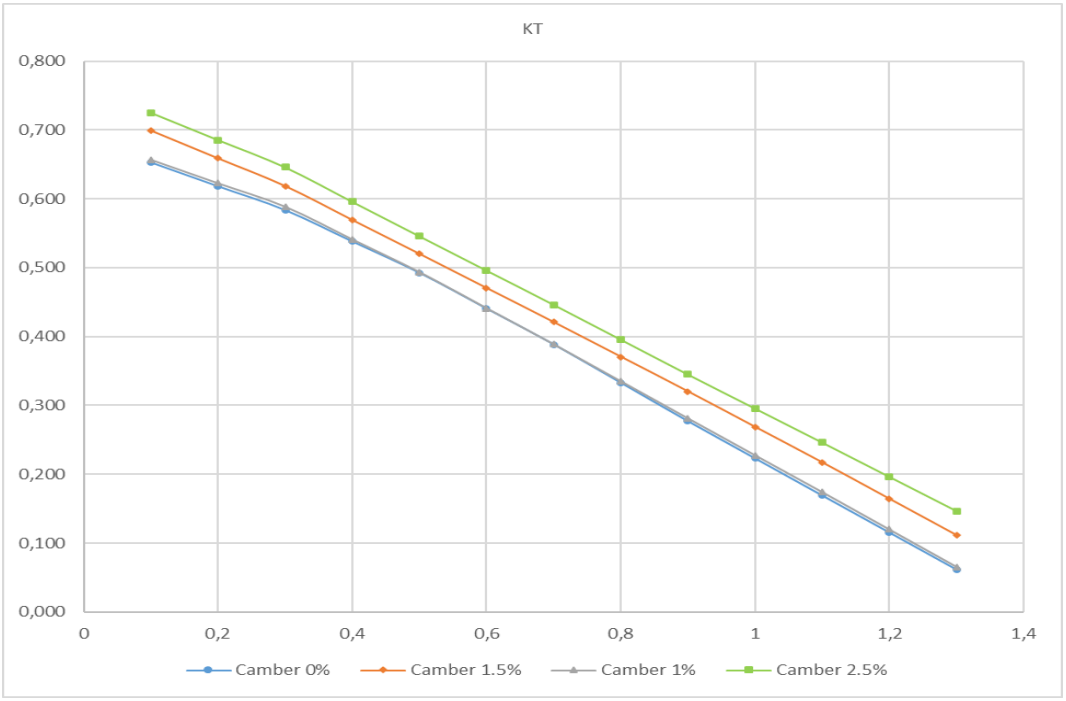

Figure. 10. Comparison of propeller thrust coefficient (KT) calculated from CFD simulations with camber ratios of 0%, 1.0%, 1.5%, and 2.5%

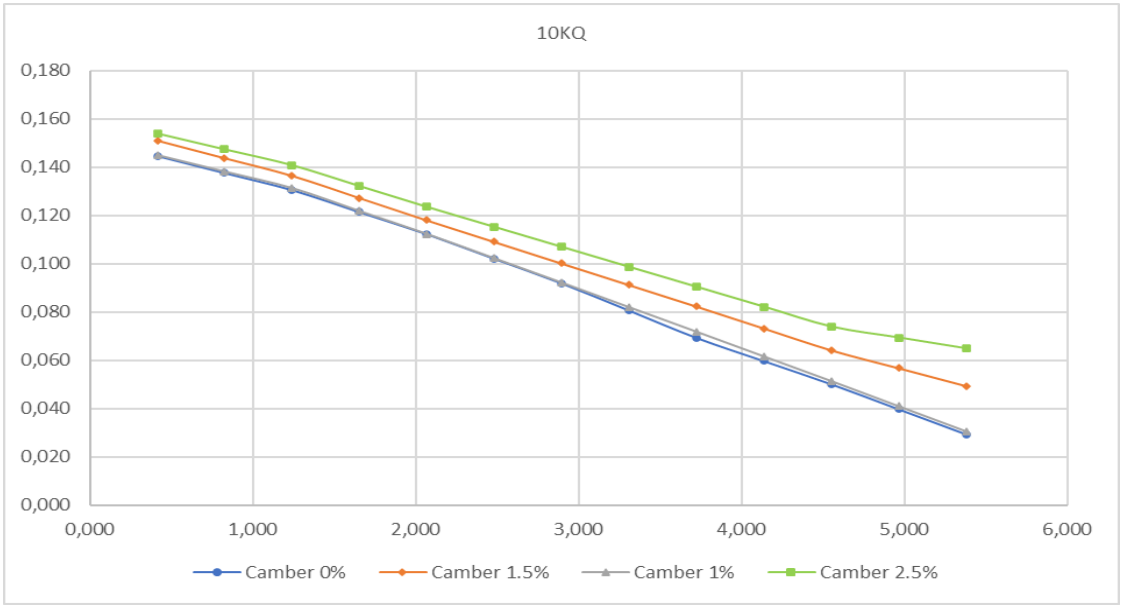

Figure. 11. Comparison of propeller torque coefficient (10KQ) calculated from CFD simulations with camber ratios of 0%, 1.0%, 1.5%, and 2.5%

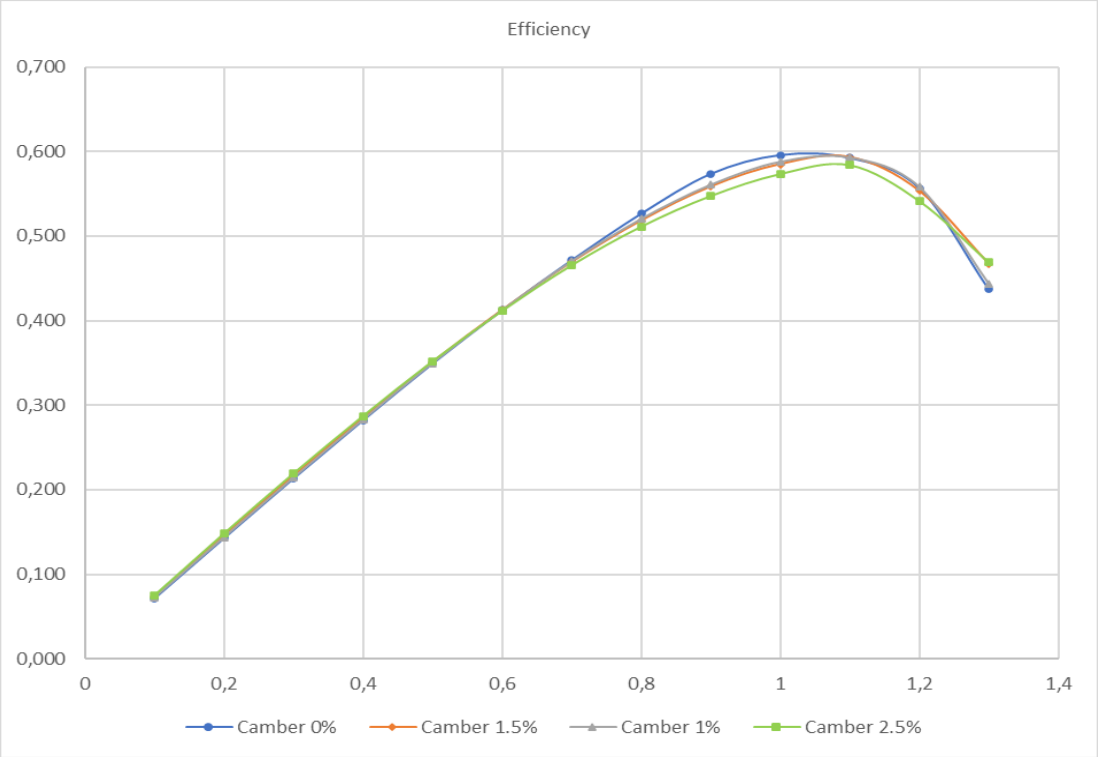

Figure. 12. Comparison of efficiency (η) obtained from CFD simulations for camber ratios of 0%, 1.0%, 1.5%, and 2.5%

At the advance coefficient J=0.9, which represents a critical operating point for evaluating propeller performance, the thrust coefficient (K_T), torque coefficient (K_Q), and open-water efficiency (η) for each camber ratio variation are summarized in **table 8**. The results indicate that the 1% camber configuration yields the highest efficiency, reaching a value of 0.596. This corresponds to an efficiency improvement of approximately 3.85% compared with the baseline propeller having 0% camber.

This improvement not only reflects the local hydrodynamic characteristics of the propeller blades but also confirms that, at J=0.9, the 1% camber configuration achieves an optimal balance between the increased thrust produced by additional sectional lift and the rise in torque associated with increased drag. Consequently, these findings reinforce that the 1% camber ratio is the most efficient among all tested variations, particularly under operating conditions near the point of maximum propeller efficiency.

TABLE 8
VALUE OF KT, KQ, AND η FOR VARYING CAMBER RATIO.

J = 0.9			
Camber ratio (f/c)	KT	KQ	η
0%	0.277	0.069	0.574
1.0%	0.294	0.071	0.596
1.5%	0.320	0.082	0.558
2.5%	0.345	0.090	0.547

The thrust coefficient (KT) is closely associated with the pressure distribution over the propeller blade surface, as illustrated in Figure 15. Variations in the camber ratio modify the sectional geometry of the blade, thereby altering the pressure differential between the pressure side and the suction side. Increasing the camber generally enhances the pressure gradient near the leading-edge region, which in turn increases the hydrodynamic lift generated by the blade section and results in higher KT values. Consequently, the modification of pressure distribution induced by camber variation constitutes one of the primary mechanisms responsible for the increase in thrust observed at higher camber configurations.

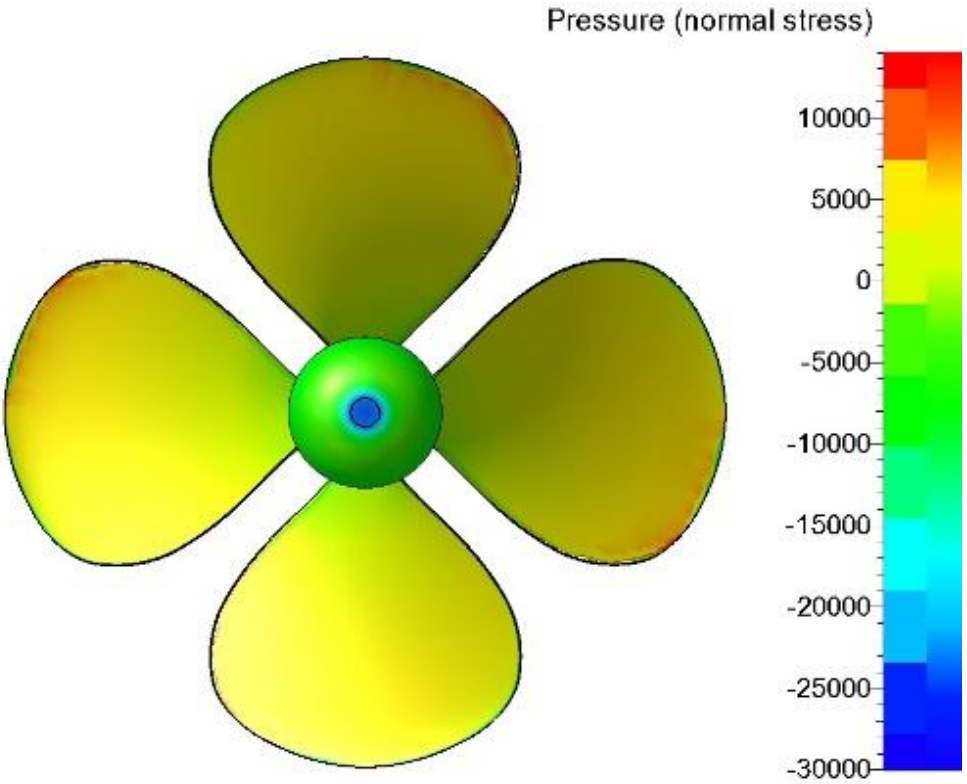
Pressure (normal stress)
10000
5000
0
-5000
-10000
-15000
-20000
-25000
-30000

(a)

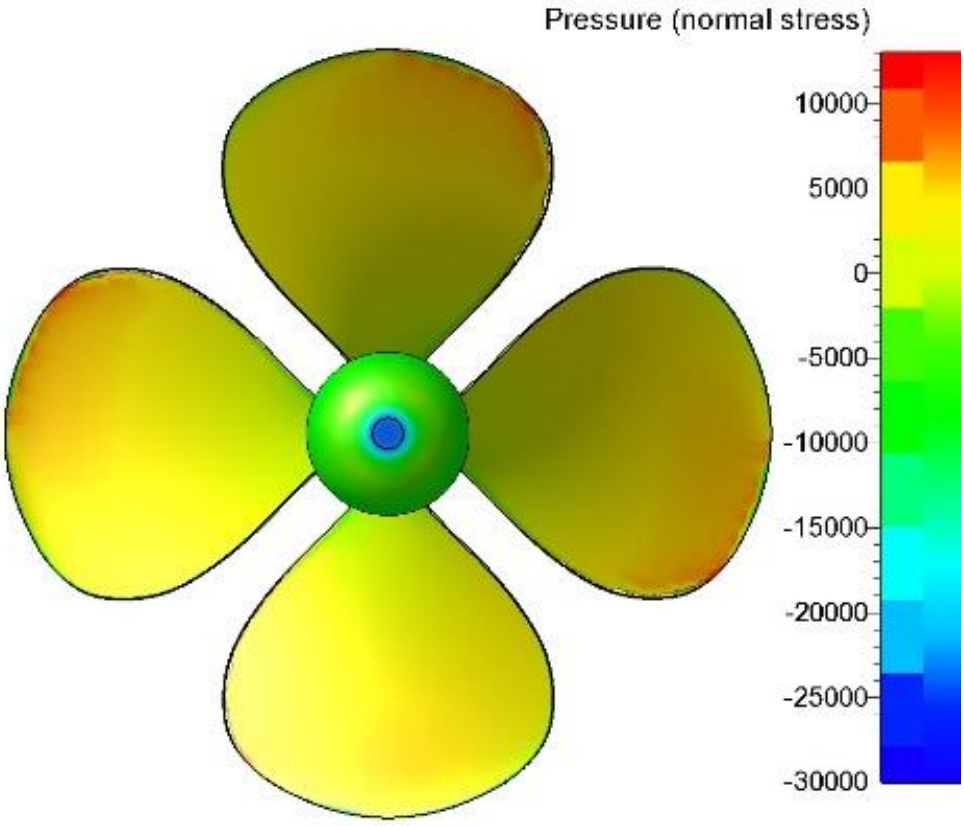
Pressure (normal stress)
10000
5000
0
-5000
-10000
-15000
-20000
-25000
-30000

(b)

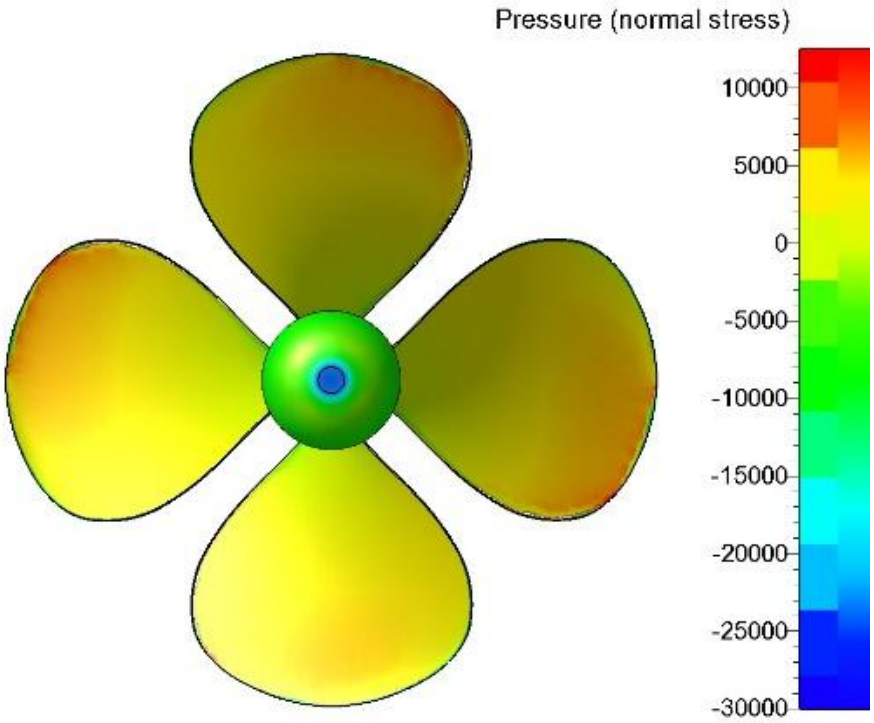

(c)

Figure. 13. Pressure distribution on the propeller blade surface at an advance coefficient of J = 0.9 for camber ratios of 1.0% (a), 1.5% (b), and 2.5% (c), presented as gauge pressure.

Figure. 13 further illustrates that increasing the camber ratio leads to higher pressure levels on the blade surface. The elevated pressure directly contributes to the increase in propeller thrust. In addition, the rotation of the propeller about the x-axis induces variations in the local flow velocity, as depicted in **Figure. 14**. These changes reveal a clear acceleration of the flow on the suction side and a deceleration on the pressure side, which constitute the primary mechanisms of thrust generation across all camber variations. This flow visualization provides additional evidence of how camber affects the local hydrodynamic characteristics surrounding the blade, reinforcing the role of camber modification in shaping overall propeller performance.

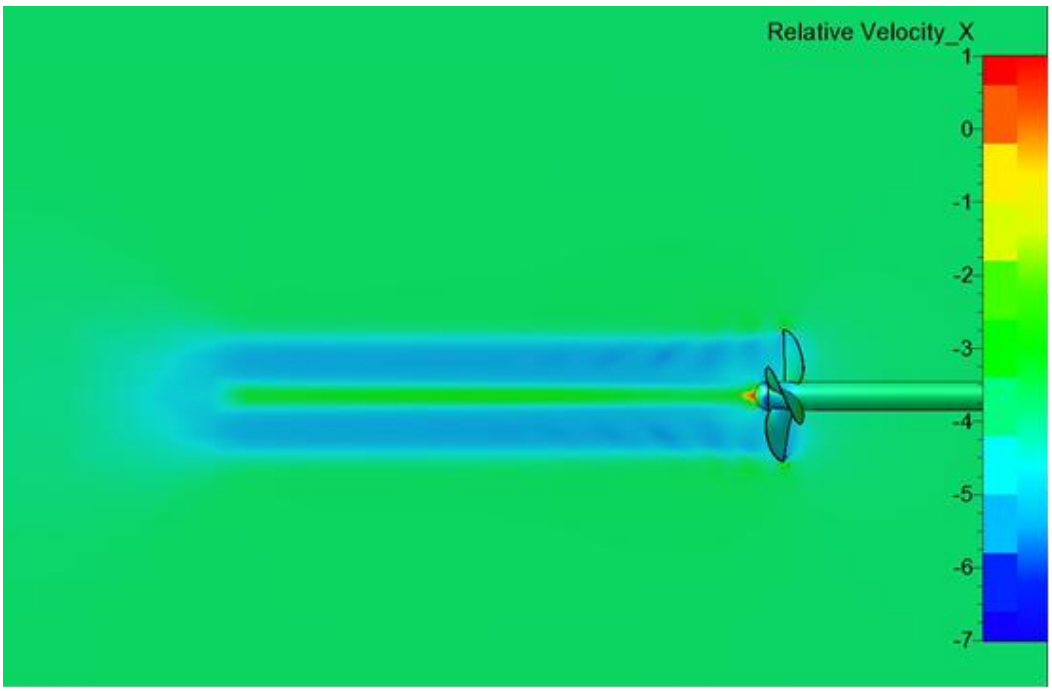

(a)

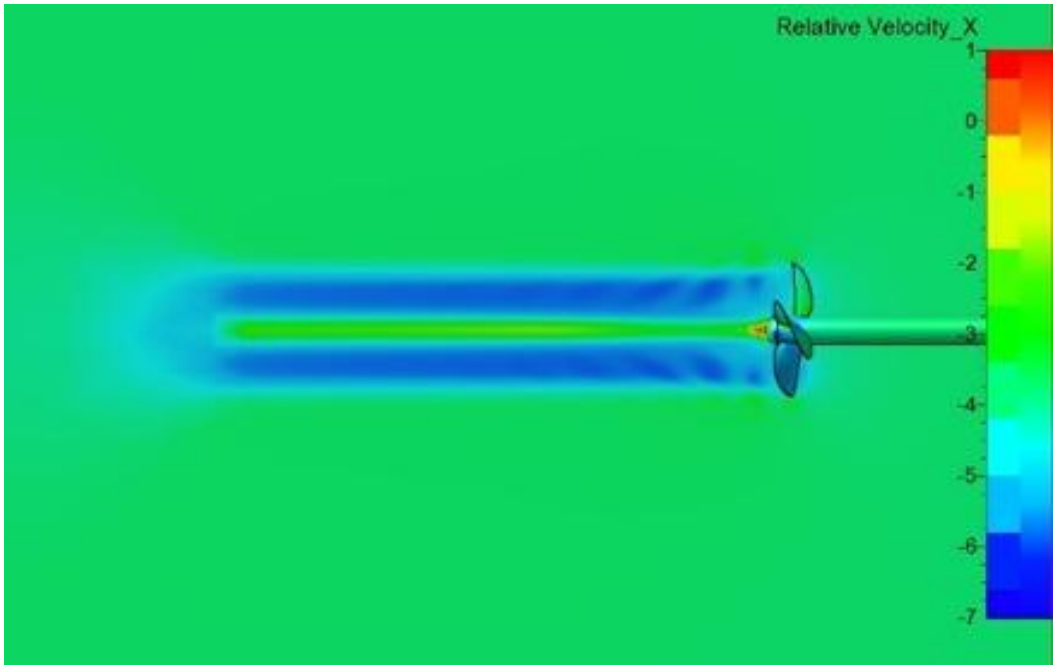

(b)

Figure. 14. Axial relative velocity at J = 0.9 with camber ratio 0% (a) and 1.0% (b).

Figure 16 illustrates that the flow velocity distribution around the propeller increases noticeably as the camber ratio is raised. For the configuration without camber (0%), the maximum flow velocity is approximately 5 m/s, whereas for the 1% camber variation this value rises to about 6 m/s. This increase occurs predominantly on the suction side of the blade, where the camber modification enhances the local flow acceleration due to the leading-edge suction effect.

The rise in flow velocity directly contributes to the increase in propeller thrust. This observation is consistent with the earlier KT analysis, in which the 1% camber configuration produced the highest thrust. Therefore, the altered flow–velocity pattern provides additional hydrodynamic evidence that the 1% camber variation maximizes the net lifting forces generated by the propeller blade, making it the most effective modification in this study.

III. Results and Discussion

The Engine Powering Method (EPM) assessment using Gawn Series propeller data with a 1% camber ratio indicates that this configuration delivers the most stable performance compared with the other camber variations evaluated in this study. Based on the open water test (OWT) results, the 1% camber modification provides an optimal balance between the increase in thrust and the corresponding rise in torque caused by the geometric alteration of the blade camber.

In general, the effects of camber augmentation on propeller performance include:

1. an increase in the local sectional lift coefficient
2. a corresponding rise in drag, which may reduce efficiency when the camber becomes excessively large

For the 1% camber configuration, the characteristics of $K_T(\theta)$and $K_Q(\theta)$demonstrate that the open-water efficiency $\eta_0$remains within the optimal range for the vessel's operating speed (26–30 knots). This stability of efficiency makes the 1% camber variation more suitable than the higher-camber alternatives. The consistent efficiency behavior also indicates that a 1% camber produces a more balanced propeller load, avoiding the excessive torque penalties observed in the higher camber cases.

A. Engine Propeller Matching

The subsequent analysis includes the calculation of propulsive power at various ship speeds, evaluation of the load curve compatibility with the engine envelope, and assessment of fuel consumption and emissions. Propeller power estimation was carried out within the operating speed range of 26–30 knots, as presented in Table 8 and Table 9. The thrust and torque values obtained from the open-water tests (OWT) of the 0% and 1% camber configurations were used to determine the brake horsepower (BHP) and propeller load (kW). Based on the values of J, KT, and KQ, the required propulsive power for each operating speed was calculated using the following formulation:

$$Va = Vs(1 - w) \quad (19)$$

$$Npropeller = \frac{Va}{.J\ x\ D} \quad (20)$$

$$DHP = 2\ x\ \pi\ x\ n \quad (21)$$

$$SHP = 95\%DHP \quad (22)$$

$$BHP = 85\%SHP \quad (23)$$

TABLE 9
ENGINE POWER REQUIRED BASED ON 0% CAMBER VARIATION

Vs (Kn)	Propeller (RPM)	Engine (RPM)	DHP (kW)	SHP (kW)
26	492	1788	3609	3798
27	505	1835	3894	4099
28	520	1892	4268	4492
29	538	1955	4640	4884
30	554	2016	5017	5281

TABLE 10
ENGINE POWER REQUIRED BASED ON 1% CAMBER VARIATION

Vs (Kn)	Propeller RPM	Engine RPM	DHP (kW)	SHP (kW)
26	492	1759	3534	3720
27	505	1820	3868	4071
28	520	1888	4245	4468
29	538	1944	4620	4863
30	554	1999	5002	5266

Figure. 15. Power requirement for each camber ratio variation (1% and 2%)

The comparison of power requirements for the two camber variations, 0% and 1%, reveals that the 0% camber propeller consistently demands slightly higher power than the 1% configuration. The difference, however, remains minimal across the tested operating points. The percentage deviations in required power between the two variants are 2.1% at 492 RPM, 0.7% at 505 RPM, 0.5% at 520 RPM, 0.4% at 538 RPM, and 0.3% at 554 RPM.

Figure. 16 present the engine–propeller matching results based on the propeller load curves and the engine envelope for the 0% camber configuration. At 2100 RPM, the installed propulsion system consists of two engines, each rated at 3900 kW, providing a total maximum continuous rating (MCR) of 7800 kW. Under these conditions, the available engine power at MCR significantly exceeds the propeller load requirement; at 554 RPM, the propeller with 0% camber ratio demands approximately 6213 kW, indicating a comfortable power margin for low to high speed operation. Meanwhile at 554 RPM, the propeller load for the 1% camber configuration reaches approximately 6195 kW, approaching the upper limit of the installed engine capacity (MCR ≈ 7800 kW for a 2 × 3900 kW configuration). This indicates that the 1% camber propeller utilizes the available engine power more effectively while remaining within the safe operational limits of the propulsion system.

At the service speed of 28 knots, the propeller with a 0% camber ratio requires approximately 68% of the engine's Maximum Continuous Rating (MCR), while the propeller with a 1% camber ratio utilizes about 67% of the available MCR. This indicates that the 1% camber configuration provides a marginal yet meaningful reduction of 1% in propeller load compared with the symmetric foil. The decrease in required propeller power for the 1% camber variation aligns with the open water test results, which demonstrated that this configuration achieves the most favorable balance between thrust and torque. Consequently, the improved hydrodynamic balance achieved by the 1% camber ratio directly translates into higher propulsive efficiency.

B. SFOC and Fuel Consumption

The Specific Fuel Oil Consumption (SFOC) values were obtained directly from the engine envelope chart corresponding to each operating point of the propeller. Meanwhile, the overall fuel mass consumption was calculated using the following expression.

$$\dot{m}f = P\ x\ \frac{SFOC}{1000} \tag{24}$$

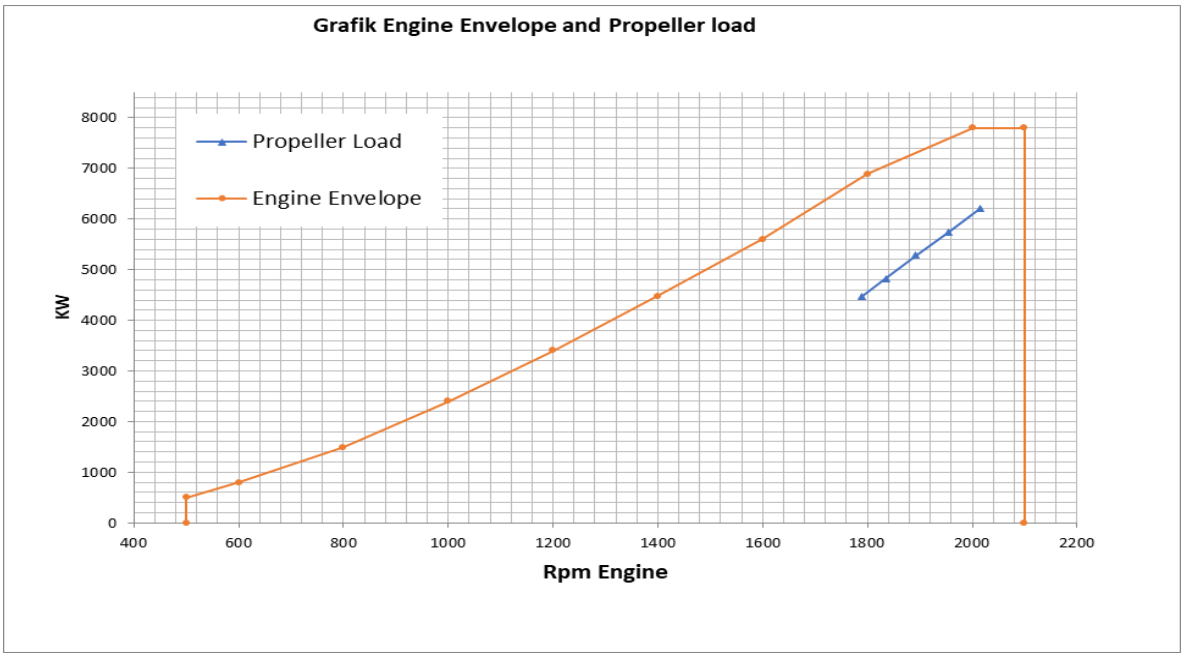

Figure. 16. Engine–propeller matching for the propeller with a 1% camber ratio

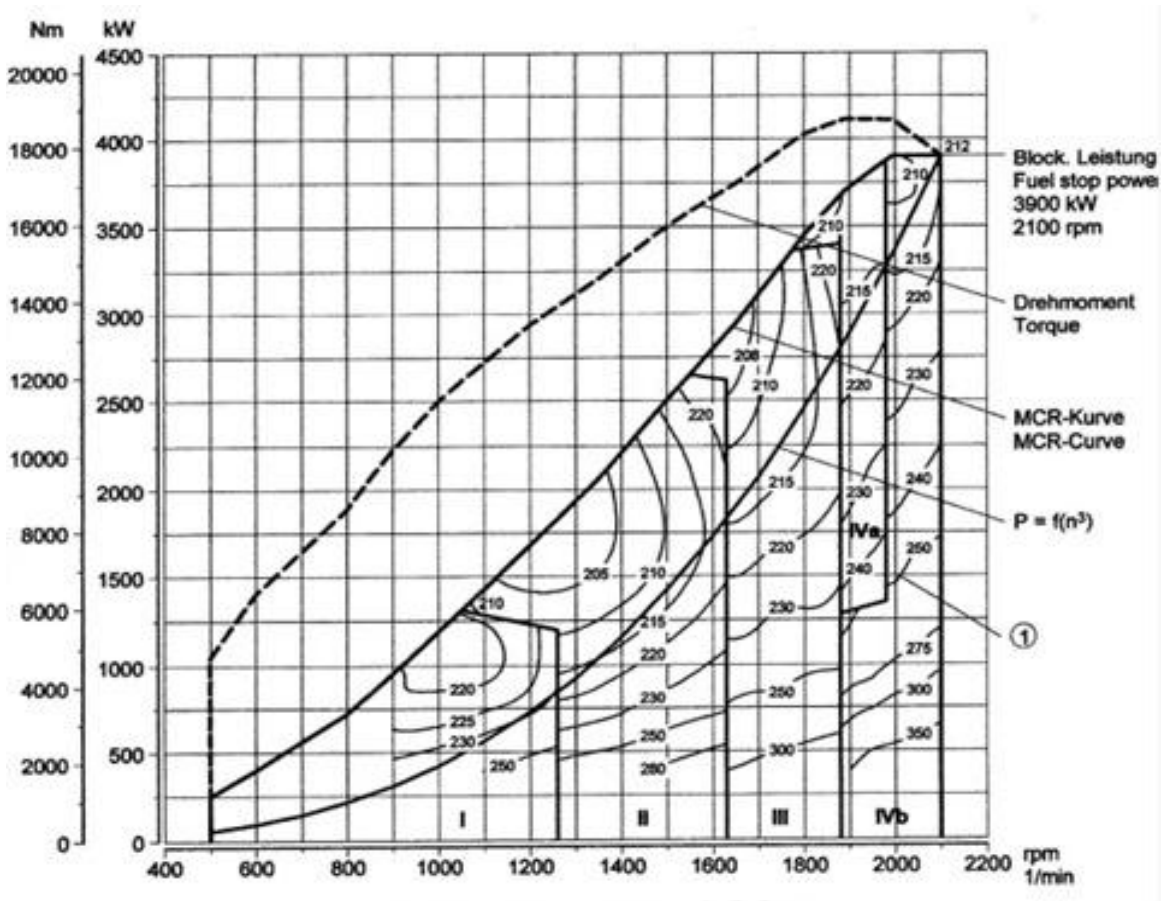

Figure. 17. Engine envelope and SFOC graph

TABLE 11
FUEL CONSUMTION ON PROPELLER VARIATION WITH CAMBER RATIO 0%.

Vs knots	N prop x GB Rpm	Prop Load kW	2 x Prop Load kW	SFOC g/BkW-hr	2 x SFOC g/BkW-hr	Feul Comp kg/hr	CO2 Emm $KgCO^2/hr$
26	492	2234.38	4469	210.0	420	1876.88	6017.27
27	505	2411.36	4823	215.0	430	2073.77	6648.51
28	520	2642.59	5285	206.0	412	2177.50	6981.06
29	538	2873.14	5746	206.0	412	2367.46	7590.09
30	554	3106.39	6213	206.0	412	2559.66	8206.28

TABLE 12
FUEL CONSUMTION ON PROPELLER VARIATION WITH CAMBER RATIO 1%

Vs knots	N prop x GB Rpm	Prop Load kW	2 x Prop Load kW	SFOC g/BkW-hr	2 x SFOC g/BkW-hr	Feul Comp kg/hr	CO2 Emm $KgCO^2/hr$
26	484	2188.40	4377	210.0	420	1838.25	5893.44
27	501	2394.77	4790	215.0	430	2059.50	6602.77
28	519	2628.44	5257	206.0	412	2165.83	6943.66
29	535	2860.63	5721	206.0	412	2357.16	7557.05
30	550	3097.48	6195	206.0	412	2552.32	8182.75

Table 10 dan Table 11 indicate that the SFOC decreases as the engine speed approaches its optimal efficiency range, which occurs between 519 and 550 rpm. Fuel consumption increases in a nearly linear manner with the propulsive power, consistent with the characteristics of high-speed diesel engines. At 30 knots, the fuel consumption reaches its highest value, amounting to 2559.66 kg/h for the 0% camber configuration. A similar increasing trend is observed for the 1% camber propeller; however, the corresponding fuel consumption remains slightly lower, recorded at 2552.32 kg/h. These results indicate that the 1% camber propeller enables the engine to operate closer to its optimal efficiency region than the 0% camber propeller, thereby reducing fuel usage at comparable operating conditions.

IV. CONCLUSION

The present study investigated the propulsion performance of a high-speed vessel using an Engine–Propeller Matching (EPM) framework, with particular attention given to the influence of propeller camber ratio on powering characteristics and fuel consumption. The analysis was conducted by combining open-water test (OWT) results with EPM evaluation to identify the most favorable propeller configuration under realistic operating conditions.

The results indicate that the propeller with a 1% camber ratio consistently exhibits superior performance compared to the other configurations examined. Across the advance-ratio range corresponding to vessel operating speeds of 26–30 knots, the 1% camber propeller demonstrates stable thrust and torque characteristics, as reflected by the behavior of the K_T(J) and K_Q(J) curves, together with a consistently high open-water efficiency. While increasing camber ratio generally leads to higher thrust and torque due to enhanced sectional lift on the blade, the 1% camber configuration achieves the most effective balance between thrust augmentation and torque demand. At an advance coefficient of J = 0.9, this configuration attains a maximum open-water efficiency of $\eta_0 = 0.596$, representing an improvement of approximately 3.85% relative to the non-cambered propeller.

From the perspective of engine–propeller compatibility, the EPM analysis confirms that the load curve associated with the 1% camber propeller remains entirely below the engine operating envelope over the investigated rotational speed range of 484–550 rpm. This indicates that the propulsion system operates without overload risk and remains within the safe limits recommended for continuous engine operation. In addition, the 1% camber configuration produces a noticeable increase in surface pressure distribution and accelerates the axial flow velocity from approximately 5 m/s for the baseline propeller to around 6 m/s. This flow acceleration enhances the suction-side performance of the blade without introducing excessive hydrodynamic losses, thereby contributing to improved propulsive efficiency.

In terms of fuel consumption, the specific fuel oil consumption (SFOC) values for both camber configurations converge to a similar level at high rotational speeds, reaching approximately 206 g/kWh. Nevertheless, the 1% camber propeller consistently demonstrates marginally lower fuel consumption over the operating range, confirming its advantage in terms of overall propulsion efficiency. Based on these findings, the 1% camber configuration offers the most balanced combination of hydrodynamic performance, engine–propeller matching, operational safety, and fuel efficiency. Accordingly, this camber ratio is recommended as the optimal design choice for Gawn Series propellers applied to high-speed vessels..

ACKNOWLEDGEMENTS

The investigation on the influence of camber ratio variations in the Gawn Series propeller was carried out through a combination of CFD-based open water simulations and Engine Propeller Matching (EPM) analysis. The study utilized a 60-m fast patrol vessel model with validated resistance and propeller test data. Propeller foil configurations with camber ratios of 0%, 1%, 1.5%, and 2.5% were evaluated based on thrust, torque, and open-water efficiency characteristics. Numerical simulations employed a scaled 1:15.03 propeller model. The resulting performance curves were

matched against engine loading characteristics of a dual-engine propulsion system rated at 2 × 3900 kW. The findings show that the 1% camber configuration consistently provides the most balanced hydrodynamic performance, lower propeller load, improved fuel consumption, and reduced CO_2 emissions across the operating speed range of 26–30 knots.

REFERENCES

[1] D. L. Blount and E. N. Hubble, "Sizing Segmental Section Commercially Available Propellers for Small Craft Propellers," in *Proceedings of the 8th Symposium*, Virginia Beach, USA: SNAME, 1981, pp. 111–138.

[2] M. Indiaryanto, I. K. Suastika, and T. A. Setyanto, "Analysis of camber ratio variation on B-Series propeller performance by using combined panel-vortex method and blade-element theory," *IOP Conf. Ser.: Earth Environ. Sci.*, vol. 1423, no. 1, p. 012031, Dec. 2024, doi: 10.1088/1755-1315/1423/1/012031.

[3] N. Mohammad Nouri and S. Mohammadi, "Numerical investigation of the effects of camber ratio on the hydrodynamic performance of a marine propeller," *Ocean Engineering*, vol. 148, pp. 632–636, Jan. 2018, doi: 10.1016/j.oceaneng.2017.06.026.

[4] M. Tadros, Z. Sun, and W. Shi, "Effect of Propeller Face Camber Ratio on the Reduction of Fuel Consumption," *JMSE*, vol. 12, no. 12, p. 2225, Dec. 2024, doi: 10.3390/jmse12122225.

[5] D. Radojčić, A. Simić, and M. Kalajdžić, "FIFTY YEARS OF THE GAWN-BURRILL KCA PROPELLER SERIES," *Part B*, vol. 151, 2009.

[6] *Practical Guidelines for Ship Self-Propulsion CFD, Recommended Procedures and Guidelines*, 2014.

[7] I. H. Abbott and A. E. von Doenhoff, *Theory of Wing Sections: Including a Summary of Airfoil Data*. New York, NY, USA: Dover Publications, Inc, 1959.

[8] D. C. Wilcox, "Reassessment of The Scale-Determining Equation for Advanced Turbulence Models," vol. 6, no. Engineering Turbulence Modelling and Experiments, pp. 389–398, 2005.

[9] M. I. Hendra, K. Suastika, T. A. Setyanto, and P. H. N. Prayoga, "Comparison of the Hydrodynamic Performance of Three Different Propeller Foil Types: NACA 66 (Mod), Ogival and NACA Symmetrical Section," *CFD Lett.*, vol. 17, no. 10, pp. 168–183, Apr. 2025, doi: 10.37934/cfdl.17.10.168183.

[10] G. B. Deng, P. Queutey, and M. Visonneau, "Three-Dimensional Flow Computation With Reynolds Stress and Algebraic Stress Models," in *Engineering Turbulence Modelling and Experiments*, 2005, pp. 389–398.

[11] G.-D. Stich, L. S. Fernandes, G. Kenway, J. A. Housman, and C. C. Kiris, "Validation of Actuator Disk, Actuator Line and Sliding Mesh Methods within the LAVA solver".

[12] MOLLAND, A. F. and UTAMA, I K A P., "Experimental and Numerical Investigations Into the Drag Characteristics of a Pair of Ellipsoids in Close Proximity," in *Proceedings of the Institution of Mechanical Engineers*, 2022, pp. 107–115.